High-order finite volume Hermite WENO schemes for hyperbolic conservation laws on triangular meshes[1]

Zhuang Zhao[2] and Jianxian Qiu[3]

Abstract

In this paper, we construct high-order Hermite weighted essentially non-oscillatory (HWENO) schemes for two-dimensional hyperbolic conservation laws on triangular meshes. These schemes integrate both zeroth- and first-order moments into spatial discretizations, yielding more compact stencils than same-order WENO schemes. Specifically, the third- and fifth-order HWENO schemes require only one and two layers of stencils, respectively, as opposed to the two layers needed by a third-order WENO scheme. Meanwhile, the HWENO schemes demonstrate reduced numerical errors in smooth areas and improved resolution near discontinuities. Although the HWENO schemes include two auxiliary equations, they retain a unified nonlinear reconstruction process similar to that of WENO schemes. This design choice leads to a modest increase in computational expense and algorithm complexity. Crucially, an efficient definition of smoothness indicators is introduced, based on a midpoint numerical integration of the original indicator. This streamlined definition enhances computational efficiencies on unstructured meshes and results in only minor variations in smoothness measurement between the two definitions, regardless of whether the problem is smooth or discontinuous. The HWENO schemes are distinguished by their strong practicality on triangular meshes, with efficient computation of smoothness indicators, consistent use of a single set of compact stencils, and application of artificial linear weights. Extensive numerical experiments are conducted to verify the high-order accuracy, efficiency, resolution, robustness, scale-invariance, and the effectiveness of the smoothness indicator for the proposed HWENO schemes.

Key Words: hyperbolic conservation laws, Hermite WENO scheme, triangular mesh, smoothness indicator, finite volume scheme

AMS(MOS) subject classification: 65M60, 35L65

[1]The research was partially supported by National Key R&D Program of China [Grant Number 2022YFA1004500], National Natural Science Foundation of China [Grant Number 12401541, 12471390], and Fundamental Research Funds for the Central Universities [Grant Number 20720240132].

[2]Corresponding author. School of Mathematical Sciences, Xiamen University, Xiamen, Fujian 361005, P.R. China. E-mail: zzhao@xmu.edu.cn.

[3]School of Mathematical Sciences and Fujian Provincial Key Laboratory of Mathematical Modeling and High-Performance Scientific Computing, Xiamen University, Xiamen, Fujian 361005, P.R. China. E-mail: jxqiu@xmu.edu.cn.

1 Introduction

In this paper, the third- and fifth-order Hermite weighted essentially non-oscillatory (HWENO) scheme are developed on triangular meshes, which evolve the zeroth- and first-order moments in time, subsequently incorporating them into spatial discretizations. The HWENO schemes are an evolution of weighted essentially non-oscillatory (WENO) schemes, which have been extensively utilized in the past three decades. A key distinction of HWENO schemes is their utilization of first-order moments or derivatives, in addition to solutions, resulting in more compact stencils compared to same-order WENO schemes. This usually leads to reduced numerical errors in smooth regions and improved resolutions near discontinuities, as supported by the formal studies [7, 8] on structured meshes. The finite volume HWENO scheme presented in [7] is particularly noted for its streamlined framework, which simplifies the reconstruction process to a single set of stencils. Building upon this foundation, we construct the third- and fifth-order schemes for solving the two-dimensional hyperbolic conservation laws on triangular meshes, as represented by the following equation:

$$\begin{cases} u_t + f(u)_x + g(u)_y = 0, \\ u(x, y, 0) = u_0(x, y). \end{cases}$$

The pioneering WENO scheme was initiated by Liu et al. [17] in 1994, where they combined all candidate stencils of essentially non-oscillatory (ENO) schemes [11, 12] (lower-order) to obtain a third-order accuracy in the finite volume framework (higher-order). In 1996, Jiang and Shu [15] developed a fifth-order finite difference WENO scheme, providing a general definition for smoothness indicators (SI) and nonlinear weights, with a focus on structured meshes. Friedrichs [10] extended the WENO methodology to unstructured meshes, but the resulting schemes did not exceed the accuracy of their ENO counterparts despite employing nonlinear weights. To leverage lower degree polynomials for higher-order accuracies, Hu and Shu [13] constructed third- and fourth-order schemes on triangular meshes by calculating linear weights at each reconstruction point. However, the process was complex, particularly in higher dimensions. Furthermore, the potential for negative or non-existent

values in the calculation of linear weights on unstructured meshes was noted in [19, 23], due to mesh quality variability. Later, a series of WENO schemes [6, 26, 31, 32] were developed following the approach of [10, 13], and Liu and Zhang [19] gave a hybrid approach that merged the methodologies of [10] and [13]. In a significant advancement, Zhu and Qiu [40] constructed third- and fourth-order WENO schemes for triangular meshes without the need for linear weight calculations, and surpassed the sub-stencil accuracy as in [13], which was subsequently extended to three-dimensional cases in [41]. The innovative concept has since been embraced in subsequent WENO schemes for unstructured meshes [1, 2, 14, 27, 42], as highlighted in a comprehensive review of the literature [25].

The construction of higher-order in WENO schemes necessitates the employment of an expanded stencil, which presents challenges when addressing boundary conditions on unstructured meshes. As illustrated in [42], the third-order WENO scheme requires the utilization of two layers of triangular meshes, and the fifth-order scheme escalates this to three layers. The addition of each mesh layer introduces complexities, particularly at boundaries, and the potential for mesh merging further complicates the scheme. To use a more compact stencil, a useful idea was proposed in the first HWENO scheme [21] by bringing the additional derivatives in each cell as auxiliary variables, and the variables also can be first-order moments seen in the $P_N P_M$ method [5] and the moment-based HWENO scheme [7]. However, the first-order derivatives or moments become quite large near discontinuities, potentially undermining the robustness of HWENO schemes. Hence, the first HWENO scheme [21] had to use two different sets of stencils in the spatial discretizations, and this similar procedure was used in the subsequent HWENO schemes [18, 22, 37, 38]. This strategy, which uses two sets of stencils to avoid discontinuities, is less robust than corresponding WENO schemes, characterized by the need for smaller time steps and more dependence on problem-specific conditions. In a recent development, a hybrid HWENO scheme [33] was proposed, which modifies first-order moments near discontinuities for subsequent utilization in spatial reconstructions. This proactive approach has demonstrated greater robustness than previous

methods when facing strong shocks, as evidenced by a series of studies [7, 8, 16, 28, 34, 35]. Specifically, the time step and capacity for tackling complex problems are comparable to analogous WENO schemes. Furthermore, the latest HWENO schemes [7, 8] have showed higher efficiencies and resolutions over the corresponding WENO schemes on structured meshes. Notably, the finite-volume HWENO scheme [7] maintains a unified and streamlined framework throughout its procedures, utilizing a single set of stencils as WENO schemes.

For practical applications, we develop third- and fifth-order HWENO schemes on triangular meshes, utilizing a unified single set of stencils and artificial linear weights, as demonstrated in [7]. Although formal HWENO schemes on triangular meshes were previously constructed by Zhu and Qiu [38], offering high-order accuracy with compact stencils, they necessitated complex linear weight calculations and dual stencil sets, posing challenges for implementations on unstructured meshes. Utilizing the framework outlined in [7], our approaches on triangular meshes necessitate the strategic selection of optimal candidate stencils. Despite this, a significant challenge remains: accurately computing SI, an issue also presents in WENO and HWENO schemes on unstructured meshes [1, 2, 13, 14, 19, 27, 30, 32, 38, 40, 41, 42]. SI, commonly used in two-dimensional schemes, was originally defined by Hu and Shu [13] as $\sum_{|l|=1}^{r} |\Omega|^{|l|-1} \int_{\Omega} \left(\frac{\partial^{|l|} p_m(x,y)}{\partial x^{l_1} \partial y^{l_2}} \right)^2 d\Omega$. This definition effectively measures the smoothness of binary polynomials and has been widely adopted in subsequent WENO and HWENO schemes across structured [7, 22] and unstructured [1, 2, 14, 19, 27, 32, 38, 40, 42] meshes. However, the explicit formulation of SI cannot be easily derived for unstructured meshes unless using local orthogonal basis functions, which are dependent on geometry and difficult to identify for high-degree polynomials. To address this, we adopt the midpoint numerical integration method as $\sum_{|l|=1}^{r} |\Omega|^{|l|} \left(\frac{\partial^{|l|}}{\partial x^{l_1} \partial y^{l_2}} p_m(x_i, y_i) \right)^2$ for computing SI, allowing explicit expression for natural basis functions. Formally, this new definition measures smoothness at individual points, similar to the finite difference WENO scheme [9]. It retains accuracy, supported by analytical methods [15, 24, 40], and varies from the original by an order of $\mathcal{O}(|\Omega|)$, with minimal impacts in discontinuous cases. Numerical examples 3.1 and

3.4 substantiate this, exhibiting nearly identical results across smooth and non-smooth cases with higher efficiencies.

Overall, the HWENO schemes are constructed via a series of steps. Firstly, a semi-discrete scheme is presented on triangular meshes, which aligns with that in DG methods [20, 43], utilizing $\mathbb{P}^1$ test functions, with the evolved variables being the zeroth- and first-order moments. Secondly, the moments are used to reconstruct a high-degree and four linear polynomials on a carefully selected set of candidate stencils. These polynomials are combined with nonlinear weights for spatial discretizations, with the option of artificial positive linear weights summing to one as [40]. Lastly, the third-order strong stability preserving Runge-Kutta time discretization method [7, 24] is used to advance the moments to subsequent stages. It is noteworthy that our HWENO schemes not only optimize the computation of SI but also uphold the property of scale-invariance, characteristic of both WENO and HWENO schemes [2, 4, 7]. This ensures identical nonlinear weights to a function and its scalar multiples within the same cell. Comparatively, our HWENO schemes demonstrate higher efficiencies and resolutions than the corresponding third-order WENO scheme, particularly with a single-layer stencil in the third-order HWENO schemes, thereby avoiding the issue of mesh merging. The advantages of these schemes will be detailed in subsequent sections through algorithmic descriptions and numerical tests.

The paper is organized as follows: in Section 2, the detailed implementation of the third- and fifth-order HWENO schemes on triangular meshes is introduced. Within this section, a simple and effective definition of SI is proposed, and the compact stencils in HWENO schemes can also be observed. In Section 3, extensive benchmarks are carried out to demonstrate the numerical accuracy, high resolution, robustness, scale-invariance, and effective SI of the proposed schemes. Finally, concluding remarks are given in Section 4.

2 Description of HWENO schemes on triangle meshes

In this section, we present the construction methodologies of the third- and fifth-order HWENO schemes for two-dimensional hyperbolic conservation laws on triangular meshes. The overall framework closely aligns with that presented in [7], wherein a singular set of stencils is consistently utilized. Nonetheless, adjustments are required in the selection of candidate stencils. The HWENO schemes are capable of employing artificial positive linear weights, provided their sum equals one. Still, the HWENO schemes preserve the characteristic of scale-invariance. Furthermore, we introduce a straightforward and effective definition of SI, which is specifically designed for unstructured meshes and exhibits only minor differences from the original definition in [13].

2.1 Semi-discrete HWENO scheme

We begin by examining two-dimensional scalar hyperbolic conservation laws, as defined by

$$\begin{cases} u_t + \nabla \cdot F(u) = 0, \\ u(x, y, 0) = u_0(x, y), \end{cases} \tag{2.1}$$

where $F = (f, g)$. The computational domain is tessellated into triangular meshes $\{\triangle_i\}$. To utilize additional information within each cell, we multiply the governing equation (2.1) by $\{1, \frac{x-x_i}{\sqrt{|\triangle_i|}}, \frac{y-y_i}{\sqrt{|\triangle_i|}}\}$ within the target cell $\triangle_i$. Here, $|\triangle_i|$ and (x_i, y_i) denote the area and the barycenter of $\triangle_i$, respectively. Subsequently, we compute their integral averages over the cell $\triangle_i$, yielding the corresponding set of integral equations as

$$\begin{cases} \dfrac{d\overline{u}_i}{dt} = -\dfrac{1}{|\triangle_i|}\displaystyle\int_{\partial\triangle_i} F \cdot \overrightarrow{n}\, ds \triangleq L_i^u, \\ \dfrac{d\overline{v}_i}{dt} = -\dfrac{1}{|\triangle_i|}\displaystyle\int_{\partial\triangle_i} \left(\frac{x-x_i}{\sqrt{|\triangle_i|}}F\right) \cdot \overrightarrow{n}\, ds + \frac{1}{|\triangle_i|^{3/2}}\int_{\triangle_i} f d\Omega \triangleq L_i^v, \\ \dfrac{d\overline{w}_i}{dt} = -\dfrac{1}{|\triangle_i|}\displaystyle\int_{\partial\triangle_i} \left(\frac{y-y_i}{\sqrt{|\triangle_i|}}F\right) \cdot \overrightarrow{n}\, ds + \frac{1}{|\triangle_i|^{3/2}}\int_{\triangle_i} g d\Omega \triangleq L_i^w, \end{cases} \tag{2.2}$$

in which the zeroth- and first-order moments of u are defined as $\overline{u}_i = \frac{1}{|\triangle_i|}\int_{\triangle_i} u d\Omega$, $\overline{v}_i = \frac{1}{|\triangle_i|}\int_{\triangle_i} u\frac{x-x_i}{\sqrt{|\triangle_i|}} d\Omega$, and $\overline{w}_i = \frac{1}{|\triangle_i|}\int_{\triangle_i} u\frac{y-y_i}{\sqrt{|\triangle_i|}} d\Omega$, respectively. Here, $\overrightarrow{n}$ represents the unit

outward normal vector to the boundary $\partial\triangle_i$. It is important to note that the semi-discrete scheme (2.2) is consistent with the approach taken in DG methods [20, 43], which employ $\mathbb{P}^1$ test functions. To obtain the numerical solution of Eqs. (2.2), the right-hand side terms are approximated by using Gaussian quadrature formulas. More specifically, the line integrals are discretized using a Gaussian quadrature formula along each edge, possessing

$$\int_{\partial\triangle_i} H(u)\cdot\overrightarrow{n}ds \approx \sum_{\ell=1}^{3}|\partial\triangle_{i,\ell}|\sum_{k=1}^{r_e}\sigma_k H(u)|_{y=y_{\ell,k}}^{x=x_{\ell,k}}\cdot\overrightarrow{n}_\ell. \tag{2.3}$$

Here, H represents F, $\frac{x-x_i}{\sqrt{|\triangle_i|}}F$, or $\frac{y-y_i}{\sqrt{|\triangle_i|}}F$. The pairs $(x_{\ell,k}, y_{\ell,k})$ and the scalars σ_k denote the Gaussian quadrature points and weights, respectively, along the edge $\partial\triangle_{i,\ell}$. r_e is set as 2 and 3 for the third- and fifth-order schemes, respectively. Additionally, the surface integrals are discretized by a Gaussian formula on each triangular element as

$$\int_{\triangle_i} h(u)d\Omega = |\triangle_i|\sum_{k}^{r_v}\zeta_k h(u)|_{y=y_k^G}^{x=x_k^G}, \tag{2.4}$$

where h symbolizes f or g. The Gaussian quadrature points (x_k^G, y_k^G) and the corresponding weights ζ_k are detailed in [3]. For the third- and fifth-order schemes, r_v is set to 4 and 7, respectively. Furthermore, the flux $H(u)\cdot\overrightarrow{n}_\ell$ at the point $(x_{\ell,k}, y_{\ell,k})$ in Eq. (2.3) is approximated by the local Lax-Friedrichs numerical flux as

$$H(u)\cdot\overrightarrow{n}_\ell \approx \frac{1}{2}\left[H(u^+)+H(u^-)\right]\cdot\overrightarrow{n}_\ell - \frac{\alpha}{2}\left(u^+-u^-\right), \tag{2.5}$$

where α is defined as the spectral radius of the Jacobian matrix, evaluated in the unit normal vector $\overrightarrow{n}_\ell$. The conservative variable approximations, u^- and u^+, denote the inside and outside of the boundary $\partial\triangle_{i,\ell}$ at the Gaussian point $(x_{\ell,k}, y_{\ell,k})$, respectively.

Utilizing the approximated techniques outlined in Eqs. (2.3), (2.4) and (2.5), the spatial discretization in the right terms of the semi-discrete scheme (2.2) is effectively reduced to the reconstruction of the function $u_i(x, y, t)$ at specific points. The detailed procedures for this reconstruction are elaborated in the subsection 2.3.

2.2 Time discretization

Due to the inherent presence of discontinuities in solutions to hyperbolic conservation laws, the magnitude of the first-order moments can escalate significantly in regions lacking smoothness. Hence, in a recent development, the finite volume HWENO scheme on structured meshes [7] has modified the first-order moments at each stage of the third-order strong stability preserving (SSP) Runge-Kutta time discretization method [24], where the modification uses the same information from spatial discretizations. This temporal discretization method is similarly adopted in the present work as

$$\begin{cases} \begin{bmatrix} \bar{u}_i^{(1)} \\ \bar{v}_i^{(1)} \\ \bar{w}_i^{(1)} \end{bmatrix} = \begin{bmatrix} \bar{u}_i^{n} \\ \hat{v}_i^{n} \\ \hat{w}_i^{n} \end{bmatrix} + \Delta t \begin{bmatrix} L_i^u(\bar{u}^n, \bar{v}^n, \bar{w}^n) \\ L_i^v(\bar{u}^n, \bar{v}^n, \bar{w}^n) \\ L_i^w(\bar{u}^n, \bar{v}^n, \bar{w}^n) \end{bmatrix}, \\ \begin{bmatrix} \bar{u}_i^{(2)} \\ \bar{v}_i^{(2)} \\ \bar{w}_i^{(2)} \end{bmatrix} = \frac{3}{4} \begin{bmatrix} \bar{u}_i^{n} \\ \hat{v}_i^{n} \\ \hat{w}_i^{n} \end{bmatrix} + \frac{1}{4} \left(\begin{bmatrix} \bar{u}_i^{(1)} \\ \hat{v}_i^{(1)} \\ \hat{w}_i^{(1)} \end{bmatrix} + \Delta t \begin{bmatrix} L_i^u(\bar{u}^{(1)}, \bar{v}^{(1)}, \bar{w}^{(1)}) \\ L_i^v(\bar{u}^{(1)}, \bar{v}^{(1)}, \bar{w}^{(1)}) \\ L_i^w(\bar{u}^{(1)}, \bar{v}^{(1)}, \bar{w}^{(1)}) \end{bmatrix} \right), \\ \begin{bmatrix} \bar{u}_i^{n+1} \\ \bar{v}_i^{n+1} \\ \bar{w}_i^{n+1} \end{bmatrix} = \frac{1}{3} \begin{bmatrix} \bar{u}_i^{n} \\ \hat{v}_i^{n} \\ \hat{w}_i^{n} \end{bmatrix} + \frac{2}{3} \left(\begin{bmatrix} \bar{u}_i^{(2)} \\ \hat{v}_i^{(2)} \\ \hat{w}_i^{(2)} \end{bmatrix} + \Delta t \begin{bmatrix} L_i^u(\bar{u}^{(2)}, \bar{v}^{(2)}, \bar{w}^{(2)}) \\ L_i^v(\bar{u}^{(2)}, \bar{v}^{(2)}, \bar{w}^{(2)}) \\ L_i^w(\bar{u}^{(2)}, \bar{v}^{(2)}, \bar{w}^{(2)}) \end{bmatrix} \right). \end{cases} \tag{2.6}$$

Here, the modified first-order moments are defined as $\hat{v}_i^{\#} \approx \frac{1}{|\triangle_i|} \int_{\triangle_i} u(x,y,t_{\#}) \frac{x-x_i}{\sqrt{|\triangle_i|}} d\Omega$ and $\overline{w}_i^{\#} \approx \frac{1}{|\triangle_i|} \int_{\triangle_i} u(x,y,t_{\#}) \frac{y-y_i}{\sqrt{|\triangle_i|}} d\Omega$, where # denotes n, (1), or (2) corresponding to each time stage. These moments are modified by HWENO methods, as detailed in the subsection 2.3.

2.3 HWENO reconstruction

We now present the detailed HWENO reconstruction procedure for the function $u_i(x,y,t)$ and the modified first-order moments $\hat{v}_i^{\#}$ and $\hat{w}_i^{\#}$ within the cell $\triangle_i$, using zeroth- and first-order moments $\{\overline{u}, \overline{v}, \overline{w}\}$. To conserve space, the temporal stage labels will be omitted henceforth, and the implementation process is structured into the subsequent three steps.

Step 1. Reconstruct four linear polynomials $\{p_m(x,y)\}_{m=1}^4$, and a quadratic polynomial $p_5(x,y)$ or a quartic polynomial $p_6(x,y)$.

For the sake of clarity, we rebel the target cell $\triangle_i$ and its three immediate neighbour cells

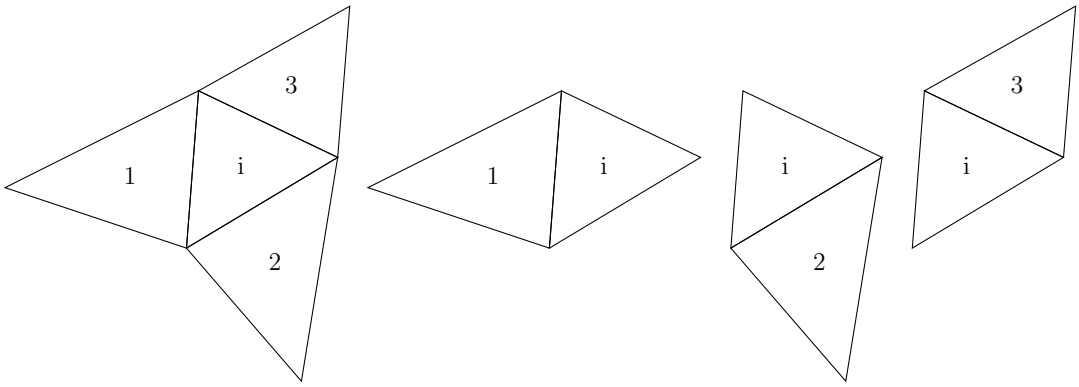

Fig. 2.1. Four small stencils $S_1, ..., S_4$ for the HWENO schemes.

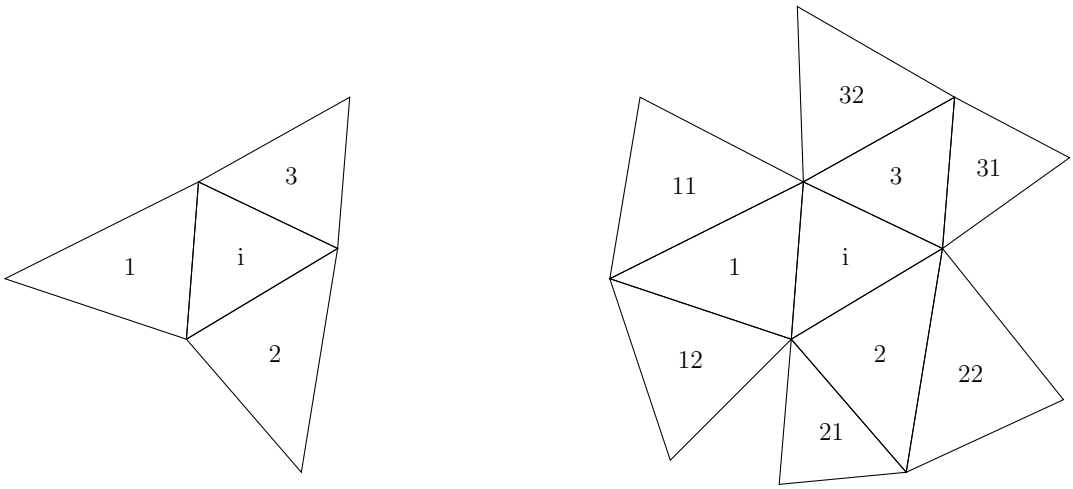

Fig. 2.2. Big stencils S_5 and S_6 for the third- and fifth-order HWENO schemes, respectively.

Table 2.1: Reconstructions of polynomials $\{p_m(x,y)\}_{m=1}^6$ on stencils $\{S_m\}_{m=1}^6$, respectively

Polynomials	Stencils	Values	Basis functions with $\xi=\frac{x-x_i}{\sqrt{\lvert\triangle_i\rvert}}$, $\eta=\frac{y-y_i}{\sqrt{\lvert\triangle_i\rvert}}$
$p_1(x,y)$	S_1	$\overline{u}_{S_1}$	$1,\xi,\eta$
$p_2(x,y)$	S_2	$\overline{u}_{S_2}$, $\overline{v}_{S_2\setminus\{i\}}$, $\overline{w}_{S_2\setminus\{i\}}$	$1,\xi,\eta$
$p_3(x,y)$	S_3	$\overline{u}_{S_3}$, $\overline{v}_{S_3\setminus\{i\}}$, $\overline{w}_{S_3\setminus\{i\}}$	$1,\xi,\eta$
$p_4(x,y)$	S_4	$\overline{u}_{S_4}$, $\overline{v}_{S_4\setminus\{i\}}$, $\overline{w}_{S_4\setminus\{i\}}$	$1,\xi,\eta$
$p_5(x,y)$	S_5	$\overline{u}_{S_5}$, $\overline{v}_{S_5\setminus\{i\}}$, $\overline{w}_{S_5\setminus\{i\}}$	$1,\xi,\eta,\xi^2,\xi\eta,\eta^2$
$p_6(x,y)$	S_6	$\overline{u}_{S_6}$, $\overline{v}_{S_6\setminus\{i\}}$, $\overline{w}_{S_6\setminus\{i\}}$	$1,\xi,\eta,\xi^2,\xi\eta,\eta^2,\xi^3,\xi^2\eta,\xi\eta^2,\eta^3,\xi^4,\xi^3\eta,\xi^2\eta^2,\xi\eta^3,\eta^4$

with the indices $i,1,2,3$. The immediate neighbour cells of $\triangle_l$, excluding $\triangle_i$ itself, are labeled as $l1$ and $l2$ on the candidate stencils $\{S_m\}_{m=1}^6$, shown in Figs. 2.1 and 2.2, where $l=1,2,3$, respectively. Here, $\overline{u}_k$, $\overline{v}_k$ and $\overline{w}_k$ represent the moments within the cell $\triangle_k$. Subsequently, we reconstruct four linear polynomials $\{p_m(x,y)\}_{m=1}^4$, a quadratic polynomial $p_5(x,y)$, and a quartic polynomial $p_6(x,y)$ on the corresponding stencils $\{S_m\}_{m=1}^6$, respectively. To facilitate clear understanding, an outline of reconstruction process for the polynomials $\{p_m(x,y)\}_{m=1}^6$ is provided in Tab. 2.1. These six polynomials $\{p_m(x,y)\}_{m=1}^6$ can be uniquely determined by ensuring they exactly match $\bar{u}_i$ for conservations, utilizing the least squares methodology as detailed in [7, 13, 36]. To streamline notation, we shall denote the subscripts "5" and "6" with the symbol "*" throughout the subsequent procedures. Later, we reformulate $p_*(x,y)$ as

$$p_*(x,y)=\gamma_*\left(\frac{1}{\gamma_*}p_*(x,y)-\sum_{m=1}^{4}\frac{\gamma_m}{\gamma_*}p_m(x,y)\right)+\sum_{m=1}^{4}\gamma_m p_m(x,y),\quad \gamma_*\neq 0. \tag{2.7}$$

To ensure the stability of the subsequent HWENO reconstruction, the set of linear weights $\{\gamma_m\}_{m=1}^6$ must be positive, with the requirement $\sum_{m=1}^4\gamma_m+\gamma_*=1$.

Step 2. Compute SI for $\{p_m(x,y)\}_{m=1}^6$, which measure the level of smoothness for each polynomial. These indicators can also be determined using the original definition from WENO and HWENO schemes [13, 19, 27, 31, 38, 40] for triangular meshes as

$$\beta_m^{\text{old}}=\sum_{|l|=1}^{r}\lvert\triangle_i\rvert^{|l|-1}\int_{\triangle_i}\left(\frac{\partial^{|l|}p_m(x,y)}{\partial x^{l_1}\partial y^{l_2}}\right)^2 d\Omega,\quad m=1,...,6, \tag{2.8}$$

where $l=(l_1,l_2)$, $|l|=l_1+l_2$, and r is the degree of $p_m(x,y)$. However, calculating these

indicators using formula (2.4) is computationally expensive even if we adjust the polynomial $\frac{\partial^{|l|}p_m(x,y)}{\partial x^{l_1}\partial y^{l_2}}$ by local orthogonal basis functions within the cell $\triangle_i$. The basis functions are dependent on geometry and are difficult to identify for high-degree polynomials. To reduce computational cost and improve practicality, we directly use the midpoint numerical integration formula to calculate it, actually computing the value of the formula (2.8) at the barycenter (x_i, y_i). This leads to a new definition of SI within the finite volume framework:

$$\beta_m = \sum_{|l|=1}^{r} |\triangle_i|^{|l|} \left(\frac{\partial^{|l|}}{\partial x^{l_1}\partial y^{l_2}} p_m(x_i, y_i) \right)^2, \quad m = 1, ..., 6. \tag{2.9}$$

Formally, this new definition measures smoothness at individual points, similar to the finite difference WENO scheme [9], but the explicit expressions of β_m can be concisely formulated as

$$\begin{cases} \beta_m = c_{m,2}^2 + c_{m,3}^2, \quad m = 1, 2, 3, 4, \\ \beta_5 = c_{5,2}^2 + c_{5,3}^2 + 4c_{5,4}^2 + c_{5,5}^2 + 4c_{5,6}^2, \\ \beta_6 = c_{6,2}^2 + c_{6,3}^2 + 4c_{6,4}^2 + c_{6,5}^2 + 4c_{6,6}^2 + 36c_{6,7}^2 + 16c_{6,8}^2 + 16c_{6,9}^2 + 36c_{6,10}^2 \\ \qquad + 576c_{6,11}^2 + 36c_{6,12}^2 + 16c_{6,13}^2 + 36c_{6,14}^2 + 576c_{6,15}^2, \end{cases} \tag{2.10}$$

where $c_{m,l}$ are the coefficients of the polynomials $\{p_m(x)\}_{m=1}^6$ based on the natural basis functions listed in Tab. 2.1.

Remark 2.1 The new definition of SI (2.9) offers several advantages over the original one (2.8). It maintains the essential properties of the original one within the finite volume framework, such as accuracy and the capacity to measure smoothness within cells, while providing more streamlined expressions and increased computational efficiencies. The reasons are given as follows. Firstly, the new definition measures the level of smoothness at the barycenter (x_i, y_i), while the original definition does so across the entire target cell. There is no essential differences for the accuracy, as supported by the analytical method of [15, 24, 40]. Secondly, the new definition can be viewed as a midpoint numerical integration of the original one, leading to that the difference between β_m and β_m^{old} is an order of $\mathcal{O}(|\triangle_i|)$ numerically. This small difference does not significantly impact the performance of two definitions in the presence of discontinuities. In such cases, both indicators reach $\mathcal{O}(1)$, indicating that their ability

to measure smoothness remains essentially unchanged. However, the streamlined expression of the new SI (2.9) translates to higher computational efficiencies on unstructured meshes, a critical advantage in practical applications. Theses properties are further illustrated by the comparison of numerical tests, as detailed in Examples 3.1 and 3.4.

Step 3. Reconstruct the solution $u_i(x,y)$ and its modified first-order moments $\hat{v}_i$ and $\hat{w}_i$ by HWENO methods.

In this step, we will introduce the nonlinear third- and fifth-order HWENO reconstructions for $u_i(x,y)$, $\hat{v}_i$ and $\hat{w}_i$, respectively. These reconstructions are capable of maintaining high-order accuracies in smooth areas while essentially ensuring non-oscillatory behaviors near discontinuities. As in the WENO and HWENO schemes [7, 34, 39, 40], a parameter τ is used to measure the overall difference between the set of $\{\beta_m\}_{m=1}^4$ and β_*, having

$$\tau = \frac{\sum_{l=1}^4 |\beta_* - \beta_l|}{4}, \tag{2.11}$$

then, the nonlinear weights are computed by

$$\omega_m = \frac{\widetilde{\omega}_m}{\sum_{l=1}^4 \widetilde{\omega}_l + \widetilde{\omega}_*}, \text{ with } \widetilde{\omega}_m = \gamma_m(1 + \frac{\tau^2}{u_{ave}^{2-p}\beta_m^p + u_{ave}^4 \varepsilon}), \ m = 1, \ldots, 4, *, \tag{2.12}$$

where $u_{ave} = \frac{\sum_{k\in S_*} \overline{u}_k}{\text{card}S_*} + 10^{-40}$, and card$S_*$ represents the count of elements in the set S_*. The incorporation of u_{ave} as a normalization procedure is essential to preserve the scale-invariant property as in the WENO and HWENO schemes [4, 7]. Here, ε is a small positive number to prevent zero denominator, and we set $\varepsilon = 10^{-8}$ in this paper. For the HWENO schemes, the parameter p is assigned as 2 for the third-order and 1 for the fifth-order, consistent with the settings in the third-order WENO scheme [2] and the fifth-order HWENO scheme [7].

Finally, a nonlinear HWENO reconstruction of the polynomial $u_i(x,y)$ for $u(x,y)$ within the target cell $\triangle_i$ is obtained by substituting a part of linear weights in (2.7) with the nonlinear weights (2.12). Concurrently, the modified first-order moments $\hat{v}_i$ and $\hat{w}_i$ are directly determined from $u_i(x,y)$ and are only used in the time discretization outlined in

(2.6). Then, we have

$$\begin{cases} u_i(x,y) = \omega_* \left(\frac{1}{\gamma_*} p_*(x,y) - \sum\limits_{m=1}^{4} \frac{\gamma_m}{\gamma_0} p_m(x,y) \right) + \sum\limits_{m=1}^{4} \omega_m p_m(x,y), \\ \hat{v}_i = \frac{1}{|\triangle_i|} \int_{\triangle_i} u_i(x,y) \frac{x-x_i}{\sqrt{|\triangle_i|}} d\Omega = \omega_* \left(\frac{1}{\gamma_*} q_*^v - \sum\limits_{m=1}^{4} \frac{\gamma_m}{\gamma_0} q_m^v \right) + \sum\limits_{m=1}^{4} \omega_m q_m^v, \\ \hat{w}_i = \frac{1}{|\triangle_i|} \int_{\triangle_i} u_i(x,y) \frac{y-y_i}{\sqrt{|\triangle_i|}} d\Omega = \omega_* \left(\frac{1}{\gamma_*} q_*^w - \sum\limits_{m=1}^{4} \frac{\gamma_m}{\gamma_0} q_m^w \right) + \sum\limits_{m=1}^{4} \omega_m q_m^w, \end{cases} \tag{2.13}$$

where $q_m^v = \frac{1}{|\triangle_i|} \int_{|\triangle_i|} p_m(x,y) \frac{x-x_i}{\sqrt{\triangle_i}} d\Omega$ and $q_m^w = \frac{1}{|\triangle_i|} \int_{|\triangle_i|} p_m(x,y) \frac{y-y_i}{\sqrt{\triangle_i}} d\Omega$. Subsequently, the values of the solution $u_i(x,y)$ at specific points are calculated to meet the needs of (2.3) and (2.4). Notably, the reconstructions presented in Eq. (2.13) are designed to achieve the third- and fifth-order accuracy when the subscript "*" is assigned to the symbols "5" and "6", respectively. The analytical procedures for the accuracy of these reconstructions are consistent with those found in the WENO schemes [15, 24, 40].

Remark 2.2 For the construction of fourth-order HWENO scheme, we are capable of directly reconstructing a cubic polynomial on the stencil S_6 utilizing the values of $\overline{u}_{S_6}$, $\overline{v}_{S_6\backslash\{i\}}$, $\overline{w}_{S_6\backslash\{i\}}$ by using the same definition of nonlinear weights (2.12) for the fifth-order HWENO scheme. However, this approach incurs some numerical wastes, as the WENO scheme [40] has demonstrated the ability to achieve fourth-order accuracies with the same stencil, under the condition that mesh merging is not performed. For the more compact stencil S_5, it is feasible to employ the values of $\overline{u}_{S_5}$, $\overline{v}_{S_5\backslash\{i\}}$, $\overline{w}_{S_5\backslash\{i\}}$ in the reconstruction process, resulting in a cubic polynomial. Nevertheless, the final HWENO scheme loses its accuracy as the mesh undergoes refinement.

Remark 2.3 For systems such as the two-dimensional compressible Euler equations, the HWENO procedures are initially used in cooperation with the local characteristic decomposition on the directions provided by two fluxes, respectively, yielding two distinct sets of values. Subsequently, a simple average of these sets is computed to obtain the approximate values. These approximations are finally used in the semi-discrete scheme (2.2) and the time discretization (2.6).

3 Numerical tests

In this section, we present the numerical results to validate the third- and fifth-order accuracy, efficiency, high resolution, and robustness of the proposed HWENO schemes, denoted as the HWENO3 and HWENO5 schemes, respectively. For comparisons, we also present the results of a third WENO scheme, referred as the WENO3 scheme. The WENO3 scheme employs the same nonlinear weights definition as the HWENO3 scheme but utilizes the candidate stencils from the third-order WENO scheme of Zhu and Qiu [40]. It should be noted that, despite both achieving the third-order accuracy, the stencil for the WENO3 scheme is wider than that for the HWENO3 scheme. Moreover, the higher-order HWENO5 scheme employs the same big stencil as the WENO3 scheme. The linear weights of the four linear polynomials $\gamma_{1,\ldots,4}$ are set as 0.01 with the remainder allocated to 0.96, following the recommendations of [40]. This allocation effectively balances the accuracy, resolution and robustness for the numerical tests presented. The Courant-Friedrichs-Lewy (CFL) number is set as 0.6. Besides, the simulations were conducted on the environment of Inter(R) Xeon (R) Gold 6130 CPU @ 2.10 GHz using Fortran 95 as the programming language, and the computational meshes are generated by the software COMSOL Multiphysics 5.3.

3.1 Accuracy tests

In this subsection, we initially validate the accuracy of the proposed HWENO3 and HWENO5 schemes on the sample mesh depicted in Figure 3.1, as well as on its refined meshes. It should be noted that the refinement process involves subdividing each element into four equivalent sub-elements uniformly across all examples. Subsequently, we compare the numerical results to demonstrate the higher efficiency of our proposed schemes over the WENO3 scheme, despite using more time in the HWENO schemes. Lastly, we confirm that the newly proposed SI (2.9) exhibits nearly equivalent performances to its original one (2.8) in smooth cases.

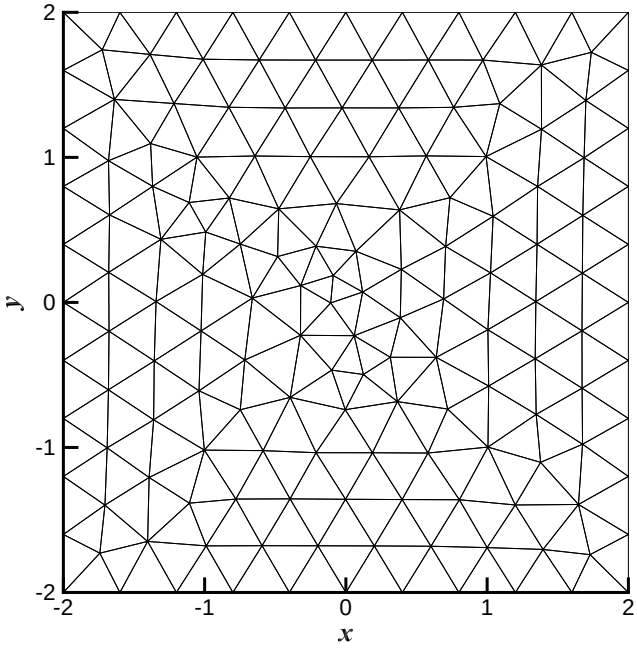

Fig. 3.1. Sample mesh for accuracy tests. Triangles: 268. Vertexes: 155.

Example 3.1 We consider the two-dimensional nonlinear Burgers' equation with the initial conditions:

$$\begin{cases} u_t + (\frac{u^2}{2})_x + (\frac{u^2}{2})_y = 0, \quad (x,y) \in [-2,2] \times [-2,2], \\ u(x,y,0) = 0.5 + \sin(0.5\pi(x+y)), \end{cases} \tag{3.1}$$

where periodic boundary conditions are implemented in each direction. We simulate this problem for the final time $T = 0.5/\pi$, at which the solution remains smooth. Firstly, we present the L^1 and L^∞ numerical errors and orders of the WENO3, HWENO3 and HWENO5 schemes in Tab. 3.1, utilizing both the newly proposed and original SI, as defined by Eqs. (2.9) and (2.8), respectively. The results indicate that all schemes achieve their designed order of accuracy. However, the HWENO3 and HWENO5 schemes exhibit smaller numerical errors. It is also observable that the numerical errors and orders of the listed schemes are nearly identical when employing the new and original SI, with minor differences observable only on coarser meshes. Furthermore, we present a comparison of CPU time against the L^1 and L^∞ errors for the WENO3, HWENO3 and HWENO5 schemes in Fig. 3.2. This

Table 3.1: Burgers' equation. L^1, L^∞ errors and orders of the WENO3, HWENO3, and HWENO5 schemes with the new and original SI, respectively. $T = 0.5/\pi$.

N cells	WENO3				WENO3 with original SI			
	L^1 error	order	L^∞error	order	L^1 error	order	L^∞ error	order
268	2.04E-02		8.62E-02		2.08E-02		8.74E-02	
1072	4.85E-03	2.08	3.10E-02	1.48	5.02E-03	2.05	3.18E-02	1.46
4288	4.20E-04	3.53	4.99E-03	2.63	4.36E-04	3.53	5.16E-03	2.63
17152	2.77E-05	3.92	3.68E-04	3.76	2.78E-05	3.97	3.68E-04	3.81
68608	3.52E-06	2.98	5.57E-05	2.72	3.52E-06	2.98	5.57E-05	2.72
274432	4.51E-07	2.96	7.50E-06	2.89	4.51E-07	2.96	7.50E-06	2.89
N cells	HWENO3				HWENO3 with original SI			
	L^1 error	order	L^∞error	order	L^1 error	order	L^∞ error	order
268	1.78E-02		7.63E-02		1.83E-02		7.74E-02	
1072	3.43E-03	2.37	2.12E-02	1.85	3.68E-03	2.31	2.26E-02	1.78
4288	2.19E-04	3.97	3.40E-03	2.64	2.41E-04	3.93	3.79E-03	2.58
17152	1.36E-05	4.02	1.69E-04	4.33	1.36E-05	4.15	1.69E-04	4.48
68608	1.97E-06	2.78	3.60E-05	2.23	1.97E-06	2.79	3.60E-05	2.23
274432	2.70E-07	2.86	4.94E-06	2.87	2.70E-07	2.86	4.94E-06	2.87
N cells	HWENO5				HWENO5 with original SI			
	L^1 error	order	L^∞error	order	L^1 error	order	L^∞ error	order
268	2.94E-03		3.13E-02		3.39E-03		3.18E-02	
1072	1.25E-04	4.56	2.17E-03	3.85	1.40E-04	4.59	2.47E-03	3.69
4288	3.42E-06	5.18	6.55E-05	5.05	3.62E-06	5.28	6.55E-05	5.23
17152	1.25E-07	4.78	4.99E-06	3.72	1.27E-07	4.84	4.99E-06	3.72
68608	4.63E-09	4.75	2.07E-07	4.59	4.64E-09	4.77	2.07E-07	4.59
274432	1.66E-10	4.81	8.63E-09	4.58	1.66E-10	4.81	8.63E-09	4.58

comparison reveals that the proposed HWENO schemes have higher efficiencies than the WENO3 scheme, particularly as the mesh becomes denser. Additionally, the HWENO5 scheme shows higher efficiencies compared to the HWENO3 scheme.

Example 3.2 We solve the two-dimensional compressible Euler equations:

$$\frac{\partial}{\partial t}\begin{bmatrix}\rho\\ \rho\mu\\ \rho\nu\\ E\end{bmatrix}+\frac{\partial}{\partial x}\begin{bmatrix}\rho\mu\\ \rho\mu^2+p\\ \rho\mu\nu\\ \mu(E+p)\end{bmatrix}+\frac{\partial}{\partial y}\begin{bmatrix}\rho\nu\\ \rho\mu\nu\\ \rho\nu^2+p\\ \nu(E+p)\end{bmatrix}=0, \tag{3.2}$$

in which ρ, μ, ν, E and p represent the density, velocity in the x direction, velocity in

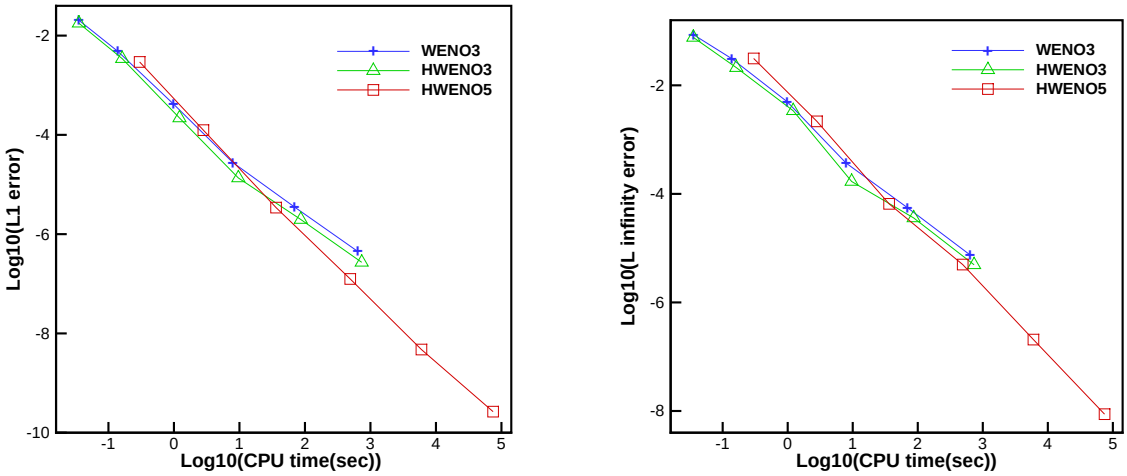

Fig. 3.2. Burgers' equation. Comparison of CPU time against L^1, L^∞ errors for Example 3.1.

the y direction, total energy, pressure, respectively. We solve this systems on the computational domain $[-2,2]\times[-2,2]$ with the initial condition given by $(\rho,\mu,\nu,p,\gamma) = (1 + 0.2\sin(0.5\pi(x+y)),1,1,1,1.4)$. Periodic boundary conditions are applied to two directions. The computation is carried out until the final time $T = 1$ with the exact solutions specified $(\rho,\mu,\nu,p) = (1+0.2\sin(0.5\pi(x+y-2T)),1,1,1)$. Firstly, we present the L^1 and L^∞ numerical errors and orders for the WENO3, HWENO3 and HWENO5 schemes in Tab. 3.2, which shows that all three schemes achieve the designed order of accuracy. It is noteworthy that the HWENO3 scheme has smaller numerical errors and more compact stencils than the WENO3 scheme, despite both achieving the same-order of accuracy. Furthermore, the HWENO5 scheme achieves a higher-order of accuracy than the WENO3 scheme, even though they employ the same big stencil. Additionally, we present the CPU time against the L^1 and L^∞ errors for the WENO3, HWENO3 and HWENO5 schemes in Fig. 3.3. This comparison intuitively reveals that the proposed HWENO schemes have higher efficiencies than the WENO3 scheme, particularly as the mesh is refined, and the HWENO5 scheme also has higher efficiencies than the HWENO3 scheme.

Table 3.2: Euler equations. L^1, L^∞ errors and orders of the WENO3, HWENO3, and HWENO5 schemes. $T = 1$.

N cells	WENO3				HWENO3			
	L^1 error	order	L^∞error	order	L^1 error	order	L^∞ error	order
268	2.31E-02		5.81E-02		1.67E-02		4.04E-02	
1072	3.79E-03	2.61	1.46E-02	1.99	2.14E-03	2.97	9.11E-03	2.15
4288	2.18E-04	4.12	9.56E-04	3.93	5.81E-05	5.20	4.58E-04	4.31
17152	2.76E-05	2.98	6.01E-05	3.99	6.26E-06	3.21	2.18E-05	4.39
68608	3.49E-06	2.99	7.44E-06	3.01	7.93E-07	2.98	3.59E-06	2.60

N cells	HWENO5			
	L^1 error	order	L^∞error	order
268	8.21E-04		3.48E-03	
1072	1.38E-05	5.90	2.16E-04	4.01
4288	2.15E-07	6.00	4.71E-06	5.52
17152	4.82E-09	5.48	4.55E-08	6.69
68608	1.45E-10	5.06	6.47E-10	6.14

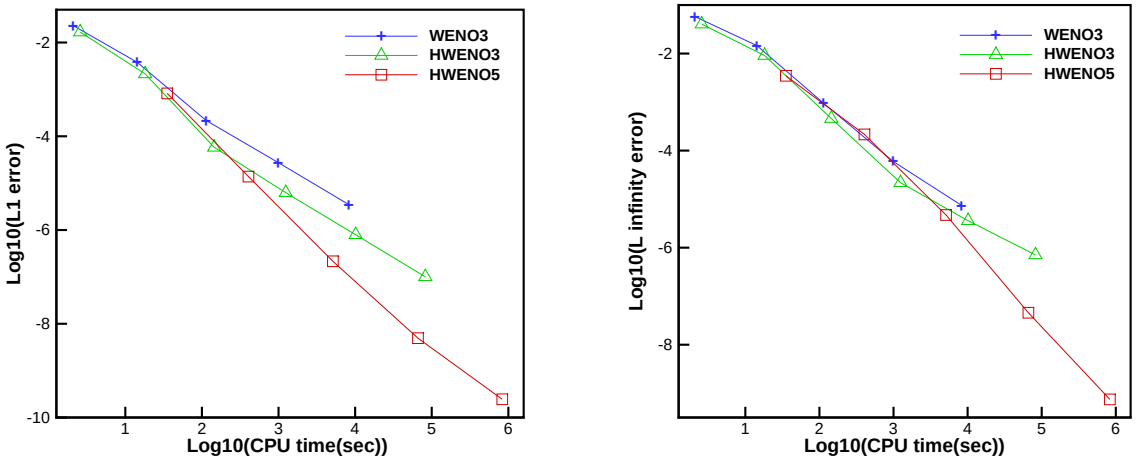

Fig. 3.3. Euler equations. Comparison of CPU time against L^1, L^∞ errors for Example 3.2.

3.2 Discontinuous tests

In this subsection, we demonstrate the performance of the proposed HWENO3 and HWENO5 schemes in the presence of discontinuities. We also evaluate the efficiency and resolution of the newly proposed SI, as defined by (2.9), as well as the scale-invariant properties of the nonlinear weights, as outlined in (2.12). For a more intuitive comparison of the results, we extend the classic one-dimensional benchmark problems-the Lax shock tube, the two-blast wave, and the Shu-Osher test-to two-dimensional settings, utilizing non-uniform computational meshes.

Example 3.3 We solve the two-dimensional Lax problem modeled by the Euler equations (3.2) with the initial conditions:

$$(\rho,\mu,\nu,p,\gamma)^{\mathsf{T}} = \begin{cases} (0.445, 0.698, 0, 3.528, 1.4)^{\mathsf{T}}, & -0.5 \le x < 0, \\ (0.5, 0, 0, 0.571, 1.4)^{\mathsf{T}}, & 0 \le x \le 0.5. \end{cases}$$

The computational domain for this problem is $[-0.5, 0.5] \times [-0.03, 0.03]$ with a final simulation time of $T = 0.16$. Outflow and periodic boundary conditions are applied to the x and y directions, respectively. This problem is simulated by the WENO3, HWENO3, and HWENO5 schemes on a nonuniform mesh with a triangulation of 100 edges in the x-direction and 6 edges in the y-direction. Firstly, we present the computed density at $y = 0$ for these three schemes in Fig. 3.4, which illustrates that the HWENO schemes offer slightly higher resolutions than the WENO3 scheme. Subsequently, we give the total computational time for these three schemes in Tab. 3.3, using both the original one (2.8) and the newly proposed SI (2.9), where we take the average time of multi-calculations as the final CPU time. The results show that the new SI can slightly reduce the total CPU time, particularly for higher-order schemes. Additionally, the CPU time for the HWENO3 scheme increases nearly 24% than that of the WENO3 scheme. Furthermore, the new definition of SI can easily obtain the explicit expression even for a very high-degree polynomial, observed in (2.10).

Example 3.4 We solve the two-dimensional two blast wave problem modeled by the Euler

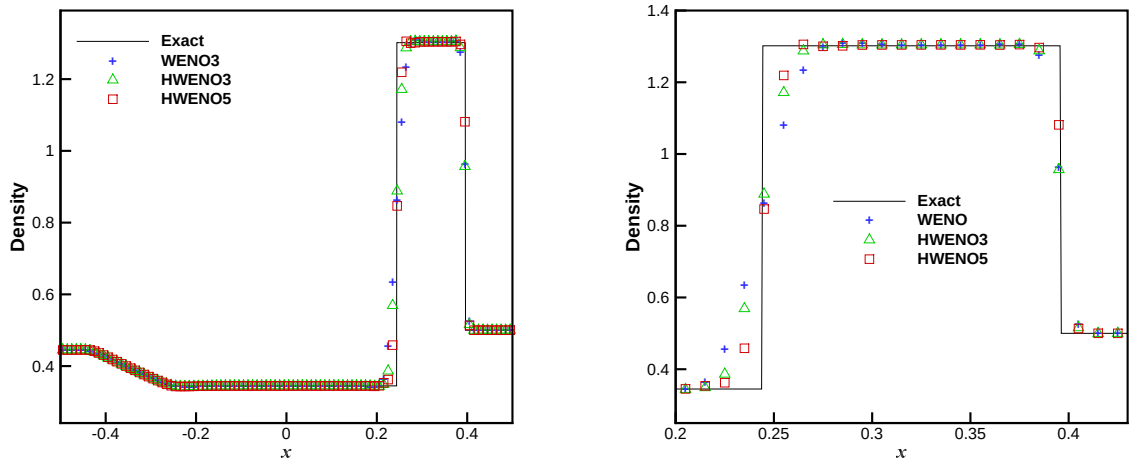

(a) Density

(b) Density Zoomed in

Fig. 3.4. Example 3.3. Lax problem. Computed density of the WENO3, HWENO3, and HWENO5 schemes at $y = 0$. Nonuniform meshes. x-direction: 100 edges. y-direction: 6 edges.

Table 3.3: Example 3.3. Lax problem. Total CPU time (s) of the WENO3, HWENO3 and HWENO5 schemes with the original and new proposed SI, respectively.

Scheme	Original SI	New proposed SI	Ratio
WENO3	89.55	85.14	95.08%
HWENO3	110.34 (+23.21%)	105.27 (+23.64%)	95.41%
HWENO5	333.99 (+272.96%)	298.22 (+250.27%)	89.29%

equations (3.2) with the initial conditions:

$$(\rho,\mu,\nu,p,\gamma)^{\mathsf{T}}=\begin{cases}(1,0,0,1000,1.4)^{\mathsf{T}}, & 0\le x<0.1,\\ (1,0,0,0.01,1.4)^{\mathsf{T}}, & 0.1\le x<0.9,\\ (1,0,0,100,1.4)^{\mathsf{T}}, & 0.9\le x\le 1.\end{cases}$$

The computational domain is set as $[0,1]\times[-0.0075,0.0075]$ with a final time of $T=0.038$. Reflective and periodic boundary conditions are applied to the x and y directions, respectively. The problem is simulated using the WENO3, HWENO3, and HWENO5 schemes on a nonuniform mesh with a triangulation of 400 edges in the x-direction and 6 edges in the y-direction. Firstly, we present the computed densities for the three schemes in Fig. 3.5 at $y=0$, demonstrating that the HWENO schemes exhibit higher resolutions than the WENO3 scheme, where the reference solution is obtained by the classical WENO scheme [15], utilizing 2001 points. Subsequently, we present the results for the three schemes using the newly proposed SI (2.9) and the original indicator (2.8), as shown in Fig. 3.7, which are nearly identical for each scheme, further indicating that the new SI possesses a comparable ability to measure the level of smoothness as the original one. Additionally, we test this problem across various scales, with the initial conditions given by $(\zeta\rho,\mu,\nu\zeta p,\gamma)$, with $\zeta=10^{\pm 12}$, and the corresponding exact solution for density at time T is $\zeta\rho(x,T)$. The results, normalized, are presented in Fig. 3.7, which are consistent for each scheme, thereby validating the scale invariance of the three schemes due to the definition of the nonlinear weights (2.12).

Example 3.5 We solve the two-dimensional Shu-Osher problem [24] modeled by the Euler equations (3.2) with the initial conditions:

$$(\rho,\mu,\nu,p,\gamma)^{\mathsf{T}}=\begin{cases}(3.857143,2.629369,0,10.333333,1.4)^{\mathsf{T}}, & -5\le x<-4,\\ (1+0.2\sin(5x),0,0,1,1.4)^{\mathsf{T}}, & -4\le x\le 5.\end{cases}$$

The computational domain is set as $[-5,5]\times[-0.1,0.1]$ with a final time of $T=1.8$. Outflow and periodic boundary conditions are applied to the x and y directions, respectively. This problem involves the interaction between shock and entropy waves, and is simulated by the WENO3, HWENO3, and HWENO5 schemes on a nonuniform mesh with a triangulation

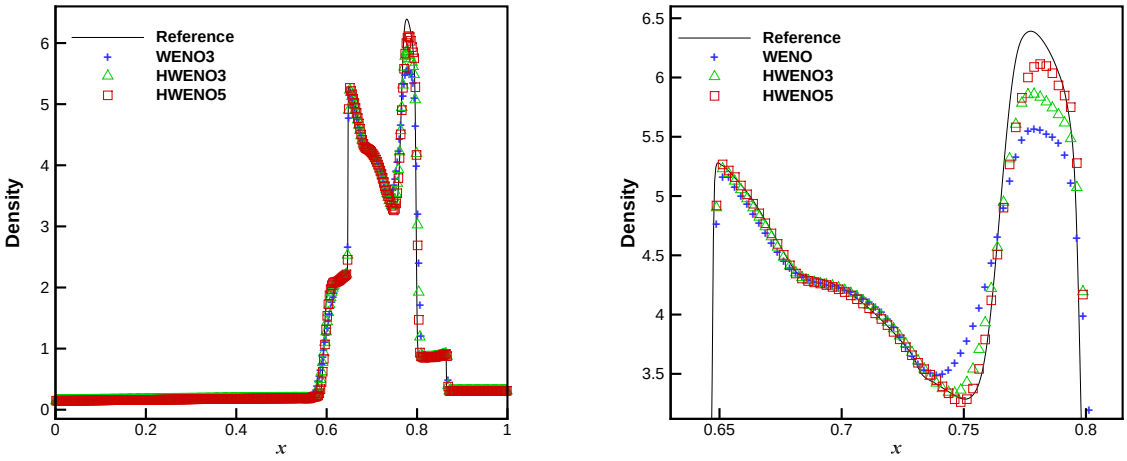

(a) Density (b) Density zoomed in

Fig. 3.5. Example 3.4. Two blast wave problem. Computed density of the WENO3, HWENO3, and HWENO5 schemes at $y = 0$. Nonuniform meshes. x-direction: 400 edges. y-direction: 6 edges.

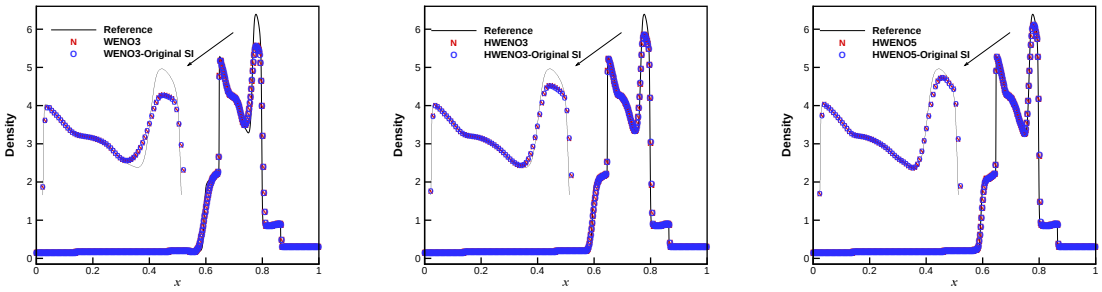

(a) WENO3 (b) HWENO3 (c) HWENO5

Fig. 3.6. Example 3.4. Two blast wave problem. Comparison of the WENO3, HWENO3, and HWENO5 schemes with the new proposed SI (2.9) and the original SI (2.8).

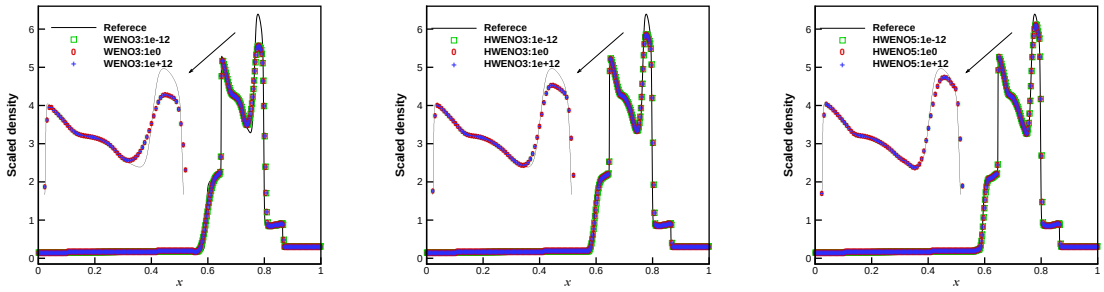

(a) WENO3 (b) HWENO3 (c) HWENO5

Fig. 3.7. Example 3.4. Two blast wave problem. Comparison of the WENO3, HWENO3, and HWENO5 schemes with various scales.

of 300 edges in the x-direction and 6 edges in the y-direction. We present the computed densities for the three schemes in Fig. 3.8, demonstrating that the HWENO schemes exhibit higher resolutions than the WENO3 scheme, where the reference solution is obtained by the classical WENO scheme [15] with 2001 points.

Example 3.6 We solve the Burgers' equation given by (3.1) in Example 3.1 using the same initial and boundary conditions on a refined mesh with 4228 triangles and 2225 vertexes as depicted in Fig. 3.1. The final computational time is set to $T = 1.5/\pi$, at which the solution exhibits discontinuities. We present the numerical results for the WENO3, HWENO3, and HWENO5 schemes in Fig. 3.9, demonstrating that the three schemes exhibit good resolutions near discontinuities on this unstructured meshes.

Example 3.7 We solve the double Mach reflection problem [29], which is modeled by the Euler equations (3.2). The computational domain is set as $[0, 4] \times [0, 1]$ and the initial condition is

$$(\rho, \mu, \nu, p, \gamma) = \begin{cases} (8, \frac{33}{4}\sin(\frac{\pi}{3}), -\frac{33}{4}\cos(\frac{\pi}{3}), 116.5, 1.4), & x < \frac{1}{6} + \frac{y}{\sqrt{3}}, \\ (1.4, 0, 0, 1, 1.4), & \text{otherwise.} \end{cases}$$

Inflow and outflow boundary conditions are applied to the left and right edges, respectively. An exact post-shock boundary condition is imposed along the bottom from $x = 0$ to $x = \frac{1}{6}$, and the remaining bottom portion is subject to a reflection boundary condition. Additionally,

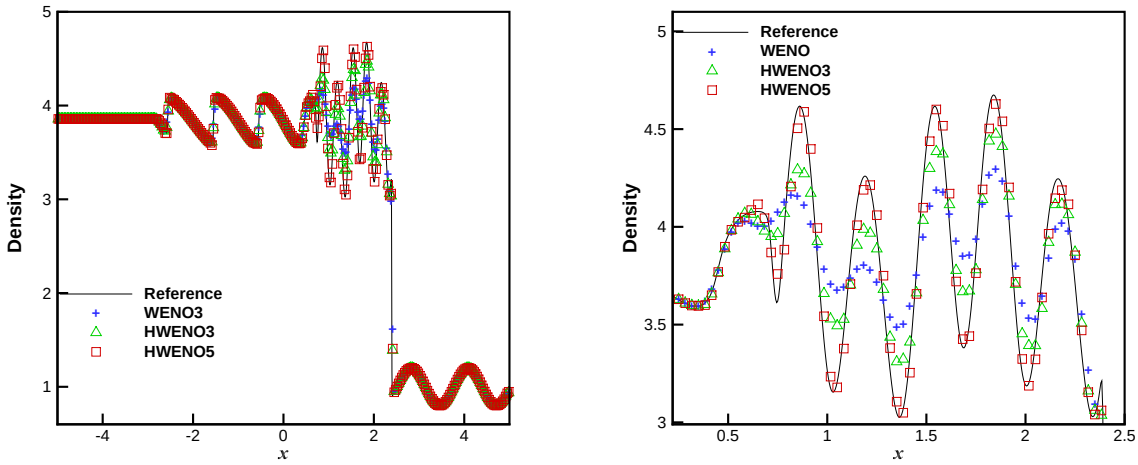

(a) Density (b) Density Zoomed in

Fig. 3.8. Example 3.5. Shu-Osher problem. Computed density of the WENO3, HWENO3, and HWENO5 schemes at $y = 0$. Nonuniform meshes. x-direction: 300 edges. y-direction: 6 edges.

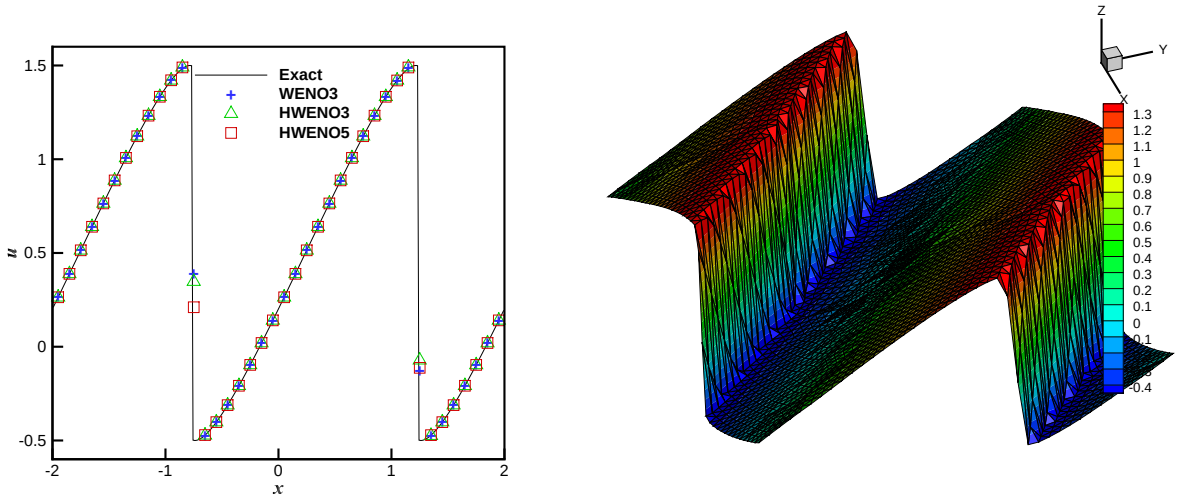

(a) Numerical solution (b) Surface of HWENO5

Fig. 3.9. Example 3.6. Burgers' problem. Numerical solution of WENO3, HWENO3, and HWENO5 schemes at $x = y$. Triangles: 4228. Vertexes: 2225.

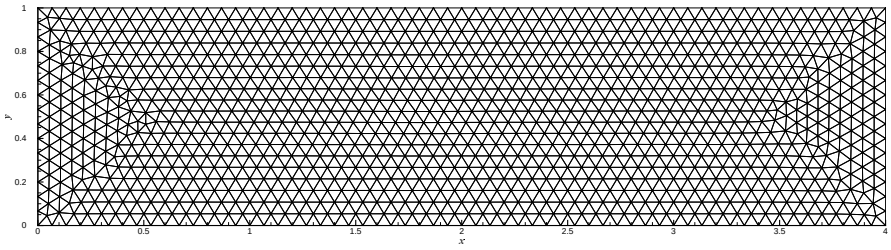

Fig. 3.10. Example 3.7. Sample mesh for double Mach reflection problem. Triangles: 2302. Vertexes: 1227.

the motion of a Mach 10 shock is applied at the top boundary. The simulation stops at a final time of $T = 0.2$ using the WENO3, HWENO3, and HWENO5 schemes on a refined mesh with 589312 triangles and 295857 vertexes, as depicted in the sample mesh of Fig. 3.10. We present the computed densities for the three schemes in Fig. 3.11, demonstrating that the HWENO schemes offer higher resolutions than the WENO3 scheme, particularly in the results obtained by the HWENO5 scheme.

Example 3.8 We finally address the forward step problem [29], which is modeled by the Euler equations (3.2) on the computational domain of $[0, 0.6] \times [0, 1] \cup [0.6, 1] \times [0.2, 1]$, featuring a Mach 3 wind tunnel incorporating a step. The initial condition consists of a rightward-propagating Mach 3 flow, with a final simulation time of $T = 4$. Reflective boundary conditions are imposed on the tunnel walls, while inflow and outflow conditions are specified on the left and right boundaries, respectively. This problem is simulated by the WENO3, HWENO3, and HWENO5 schemes on a refined mesh with a triangulation containing 164608 triangles and 82945 vertexes, as depicted in the sample mesh of Fig. 3.12. We present the computed density for the three schemes in Fig. 3.13. Similarly, the HWENO schemes demonstrate higher resolutions than the WENO3 scheme, particularly evident in the results from the HWENO5 scheme.

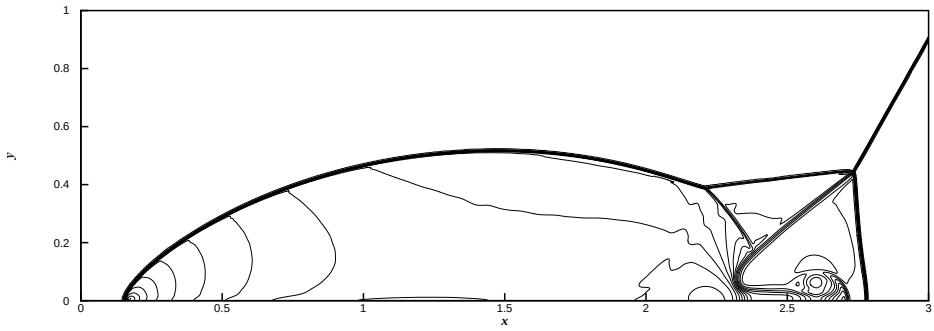

(a) WENO3

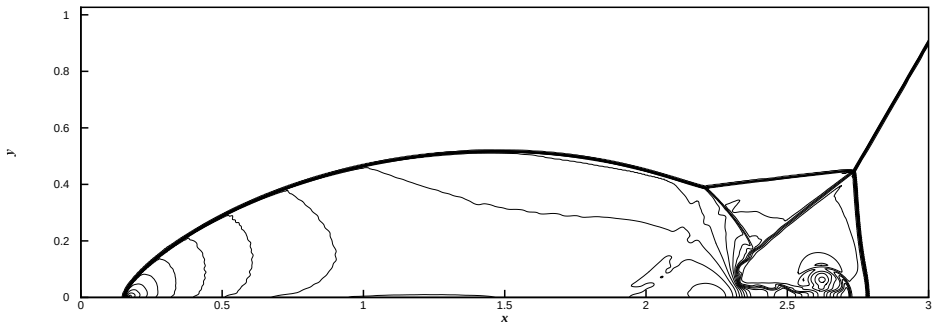

(b) HWENO3

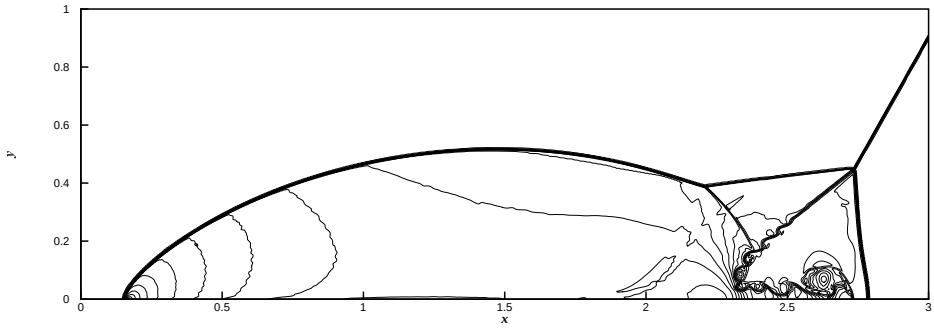

(c) HWENO5

Fig. 3.11. Example 3.7. Double Mach reflection problem. Contour plots of density with 30 equally spaced lines from 1.5 to 22.7. Triangles: 589312. Vertexes: 295857. x-direction: 960 edges. y-direction: 240 edges.

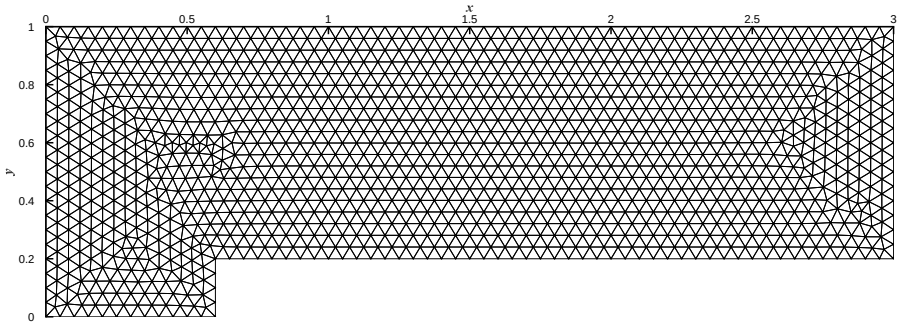

Fig. 3.12. Example 3.8. Sample mesh for step forward problem. Triangles: 2572. Vertexes: 1367.

4 Concluding remarks

In this paper, we developed the third- and fifth-order HWENO schemes for solving two-dimensional hyperbolic conservation laws on triangular meshes. The HWENO schemes employ a nonlinear combination of a high-degree polynomial and four linear polynomials within the spatial reconstruction process. This methodology not only controls spurious oscillations well but also ensures high-order accuracies, while the linear weights are unrestricted positive values, provided their sum equals one. Concurrently, these polynomials, in conjunction with nonlinear weights, have been applied into the modification of first-order moments within the temporal discretization, where the nonlinear weights keep the properties of scale-invariance as evidenced in Example 3.4. Additionally, we have implemented the midpoint numerical integration technique to compute SI, as originally defined by [13]. This approach actually provides a more straightforward and effective method for unstructured meshes, avoiding the consideration of mesh integration. Significantly, the two distinct definitions of SI exhibit minimal differences in their measurement of smoothness, regardless of whether the problem exhibits smoothness or discontinuity, as observed in Examples 3.1 and 3.4.

Compared with the corresponding third-order WENO scheme, the third-order HWENO scheme requires just a single stencil layer, while with the equivalent two layers of stencils, the HWENO scheme achieves the fifth-order accuracy. The numerical results illustrate the higher

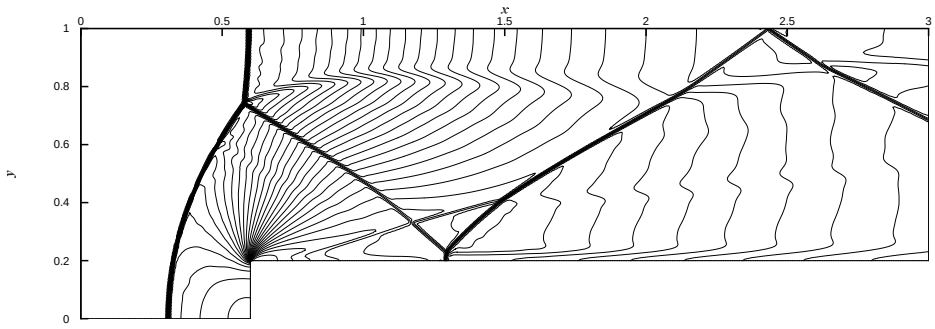

(a) WENO3

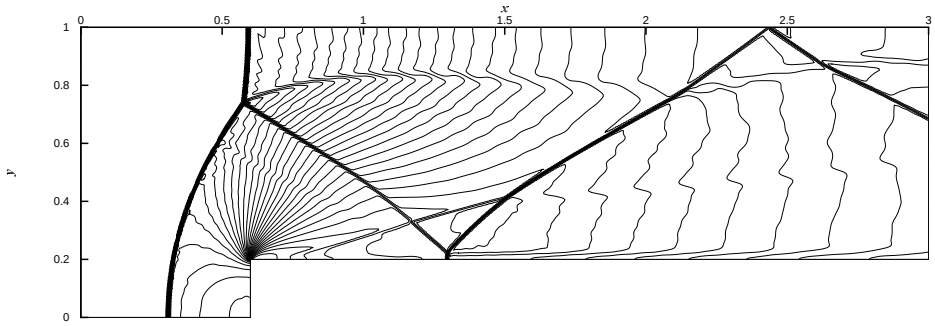

(b) HWENO3

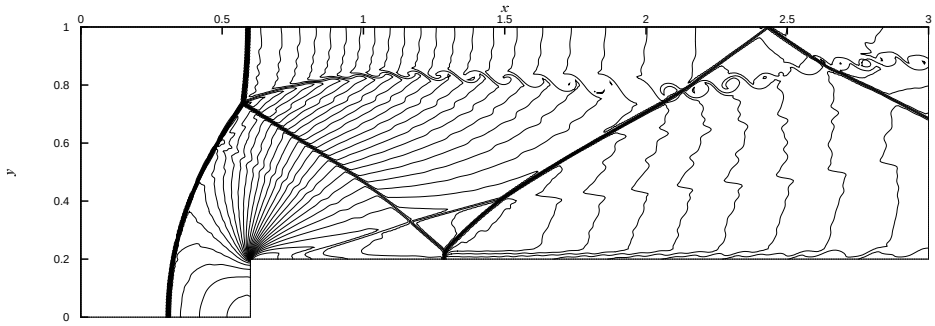

(c) HWENO5

Fig. 3.13. Example 3.8. Step forward problem. Contour plots of density with 30 equally spaced lines from 0.32 to 6.15. Triangles: 164608. Vertexes: 82945. The longest side in x-direction: 480 edges. The longest side in y-direction: 160 edges.

efficiency of the proposed HWENO schemes, characterized by diminished numerical errors and enhanced resolutions with a reduced number of transition points. It is important to note that the third-order HWENO scheme incurs only a modest in CPU expense compared to the third-order WENO scheme, as shown in Table 3.3. This is the case even though it requires two additional auxiliary equations, as indicated by Eq. (2.2). This computational cost-saving feature is attributed to the use of unified stencils, employing the same approximated polynomials and nonlinear weights, as detailed in (2.13).

Overall, these HWENO schemes present a unified and streamlined framework that is both practical and efficient for triangular meshes. This framework contains compact stencils, artificial linear weights, a streamlined formulation of SI, scale-invariant nonlinear weights, and is currently being extended to three-dimensional applications.

References

[1] D.S. Balsara, S. Garain, V. Florinski, and W. Boscheri, An efficient class of WENO schemes with adaptive order for unstructured meshes, J. Comput. Phys., 404 (2020), 109062.

[2] Y. Chen and K. Wu, A physical-constraint-preserving finite volume WENO method for special relativistic hydrodynamics on unstructured meshes, J. Comput. Phys., 466 (2022), 111398.

[3] G.R. Cowper, Gaussian quadrature formulas for triangles, Int. J. Numer. Meth. Engng., 7 (1973), 405-408.

[4] W.S. Don, R. Li, B.-S Wang, and Y. Wang, A novel and robust scale-invariant WENO scheme for hyperbolic conservation laws, J. Comput. Phys., 448 (2022), 110724.

[5] M. Dumbser, D.S. Balsara, E.F. Toro and C.D. Munz, A unified framework for the construction of one-step finite volume and discontinuous Galerkin schemes on unstructured meshes, J. Comput. Phys., 227 (2008), 8209-8253.

[6] M. Dumbser and M. Kaser, Arbitrary high order non-oscillatory finite volume schemes on unstructured meshes for linear hyperbolic systems, J. Comput. Phys., 221 (2007), 693-723.

[7] C. Fan, J. Qiu, and Z. Zhao, A moment-based Hermite WENO scheme with unified stencils for hyperbolic conservation laws, arXiv:2402.03074.

[8] C. Fan, Z. Zhao, T. Xiong, and J. Qiu, A robust fifth order finite difference Hermite WENO scheme for compressible Euler equations, Comput. Methods Appl. Mech. Engrg., 412 (2023), 116077.

[9] T.C. Fisher and M.H. Carpenter, High-order entropy stable finite difference schemes for nonlinear conservation laws: Finite domains, J. Comput. Phys., 252 (2013), 518-557.

[10] O. Friedrichs, Weighted essentially non-oscillatory schemes for the interpolation of mean values on unstructured grids, J. Comput. Phys., 144 (1998), 194-212.

[11] A. Harten, B. Engquist, S. Osher, and S. Chakravarthy, Uniformly high order accurate essentially non-oscillatory schemes III, J. Comput. Phys., 71 (1987), 231-323.

[12] A. Harten and S. Osher, Uniformly high-order accurate non-oscillatory schemes, IMRC Technical Summary Rept. 2823, Univ. of Wisconsin, Madison, WI, May 1985.

[13] C. Hu and C.-W. Shu, Weighted essentially non-oscillatory schemes on triangular meshes, J. Comput. Phys., 150 (1999), 97-127.

[14] X. Ji, F. Zhao, W. Shyy, and K. Xu, A HWENO reconstruction based high-order compact gas-kinetic scheme on unstructured mesh, J. Comput. Phys., 410 (2020), 109367.

[15] G.-S. Jiang and C.-W. Shu, Efficient implementation of weighted ENO schemes, J. Comput. Phys., 126 (1996), 202-228.

[16] J. Li, C.-W. Shu, and J. Qiu, Moment-based multi-resolution HWENO scheme for hyperbolic conservation laws, Commun. Comput. Phys., 32 (2022), 364-400.

[17] X.-D. Liu, S. Osher, and T. Chan, Weighted essentially non-oscillatory schemes, J. Comput. Phys., 115 (1994), 200-212.

[18] H. Liu and J. Qiu, Finite difference Hermite WENO schemes for conservation laws, J. Sci. Comput., 63 (2015), 548-572.

[19] Y. Liu and Y.-T. Zhang, A robust reconstruction for unstructured WENO schemes, J. Sci. Comput., 54 (2013), 603-621.

[20] H. Luo, J.D. Baum, and R. Lohner, A Hermite WENO-based limiter for discontinuous Galerkin method on unstructured grids, J. Comput. Phys., 225 (2007), 686-713.

[21] J. Qiu and C.-W. Shu, Hermite WENO schemes and their application as limiters for Runge-Kutta discontinuous Galerkin method: one-dimensional case, J. Comput. Phys., 193 (2004), 115-135.

[22] J. Qiu and C.-W. Shu, Hermite WENO schemes and their application as limiters for Runge-Kutta discontinuous Galerkin method II: Two dimensional case, Comput. Fluid., 34 (2005), 642-663.

[23] J. Shi, C. Hu, and C.-W. Shu, A technique of treating negative weights in WENO schemes, J. Comput. Phys., 175 (2002), 108-127.

[24] C.-W. Shu, Essentially non-oscillatory and weighted essentially non-oscillatory schemes for hyperbolic conservation laws, in Advanced Numerical Approximation of Nonlinear Hyperbolic Equations, B. Cockburn, C. Johnson, C.-W. Shu and E. Tadmor (Editor: A. Quarteroni), Lecture Notes in Mathematics, volume 1697, Springer, Berlin, 1998, 325-432.

[25] C.-W. Shu, Essentially non-oscillatory and weighted essentially non-oscillatory schemes, Acta Numerica, 29 (2020), 701-762.

[26] V.A. Titarev, P. Tsoutsanis, and D. Drikakis, WENO schemes for mixed-element unstructured meshes, Commun. Comput. Phys., 8 (2010), 585-609.

[27] Z. Wang, L. Tian, J. Zhu, and N. Zhao, An improved discontinuity sensor for high-order weighted essentially non-oscillatory scheme on triangular meshes, J. Comput. Phys., 490 (2023), 112299.

[28] I. Wibisono and A.K. Engkos, Fifth-order Hermite targeted essentially non-oscillatory schemes for hyperbolic conservation laws, J. Sci. Comput., 87 (2021), 1-23.

[29] P. Woodward and P. Colella, The numerical simulation of two-dimensional fluid flow with strong shocks, J. Comput. Phys., 54 (1984), 115-173.

[30] Y. Yang, L. Pan, and K. Xu, Implicit high-order gas-kinetic schemes for compressible flows on three-dimensional unstructured meshes I: Steady flows, J. Comput. Phys., 505 (2024), 112902.

[31] Y.-T. Zhang and C.-W. Shu, High order WENO schemes for Hamilton-Jacobi equations on triangular meshes, SIAM J. Sci. Comput., 24 (2003), 1005-1030.

[32] Y.-T. Zhang and C.-W. Shu, Third order WENO scheme on three dimensional tetrahedral meshes, Commun. Comput. Phys., 5 (2009), 836-848.

[33] Z. Zhao, Y. Chen, and J. Qiu, A hybrid Hermite WENO method for hyperbolic conservation laws, J. Comput. Phys., 405 (2020), 109175.

[34] Z. Zhao and J. Qiu, A Hermite WENO scheme with artificial linear weights for hyperbolic conservation laws, J. Comput. Phys., 417 (2020), 109583.

[35] Z. Zhao and J. Qiu, An oscillation-free Hermite WENO scheme for hyperbolic conservation laws, Sci. China Math., 67 (2024), 431-454.

[36] F. Zheng, C.-W. Shu, and J. Qiu, High order finite difference hermite WENO schemes for the Hamilton-Jacobi equations on unstructured meshes, Comput. Fluid., 183 (2019), 53-65.

[37] J. Zhu and J. Qiu, A class of fourth order finite volume Hermite weighted essentially non-oscillatory schemes, Sci. China Ser. A Math., 51 (2008), 1549-1560.

[38] J. Zhu and J. Qiu, Hermite WENO schemes and their application as limiters for Runge-Kutta discontinuous Galerkin method III: Unstructured meshes, J. Sci. Comput., 39 (2009), 293-321.

[39] J. Zhu and J. Qiu, A new fifth order finite difference WENO scheme for solving hyperbolic conservation laws, J. Comput. Phys., 318 (2016), 110-121.

[40] J. Zhu and J. Qiu, New finite volume weighted essentially non-oscillatory schemes on triangular meshes, SIAM J. Sci. Comput., 40 (2018), 903-928.

[41] J. Zhu and J. Qiu, A new third order finite volume weighted essentially non-oscillatory scheme on tetrahedral meshes, J. Comput. Phys., 349 (2017), 220-232.

[42] J. Zhu and C.-W. Shu, A new type of multi-resolution WENO schemes with increasingly higher order of accuracy on triangular meshes, J. Comput. Phys., 392 (2019), 19-33.

[43] J. Zhu, X. Zhong, C.-W. Shu, and J. Qiu, Runge-Kutta discontinuous Galerkin method with a simple and compact Hermite WENO limiter on unstructured meshes, Commun. Comput. Phys., 21 (2017), 623-649.